Correction and Verification of X-Ray Imaging Crystal Spectrometer Analysis on Wendelstein 7-X Through X-Ray Ray Tracing

N. Pablant,[1, a)] A. Langenberg,[2] A. Alonso,[3] M. Bitter,[1] S. Bozhenkov,[2] O. Ford,[2] K.W. Hill,[1] J. Kring,[4] O. Marchuck,[5] J. Svensson,[2] P. Traverso,[4] T. Windisch,[2] Y. Yakusevitch,[6] and the W7-X Team[b)]

[1)]*Princeton Plasma Physics Laboratory, Princeton, New Jersey 08543, USA*

[2)]*Max-Planck-Institut für Plasmaphysik, Greifswald 17491, Germany*

[3)]*Laboratorio Nacional de Fusión, CIEMAT, Madrid, 28040, Spain*

[4)]*Auburn University, Auburn, AL 36849, USA*

[5)]*Institut für Energie und Klimaforschung, Plasmaphysik, Forschungszentrum Jülich, Jülich 52425, Germany*

[6)]*University of California Santa Barbara, Santa Barbara, CA 93106, USA*

X-ray raytracing is used to develop ion-temperature corrections for the analysis of the X-ray Imaging Crystal Spectrometer (XICS) used at Wendelstein 7-X (W7-X) and perform verification on the analysis methods. The XICS is a powerful diagnostic able to measure ion-temperature, electron-temperature, plasma flow and impurity charge state densities. While these systems are relatively simple in design, accurate characterization of the instrumental response and validation of analysis techniques are difficult to perform experimentally due the requirement of extended x-ray sources. For this reason a ray-tracing model has been developed that allows characterization of the spectrometer and verification of the analysis methods while fully considering the real geometry of the XICS system and W7-X plasma. Through the use of ray-tracing, several important corrections have been found that must be accounted for in order to accurately reconstruct the ion-temperature profiles. The sources of these corrections are described along with their effect on the analyzed profiles. The implemented corrections stem from three effects: 1. effect of sub-pixel intensity distribution during de-curving and spatial binning, 2. effect of sub-pixel intensity distribution during forward model evaluation and generation of residuals, 3. effect of defocus and spherical aberrations on the instrumental response. Possible improvements to the forward model and analysis procedures are explored, along with a discussion of tradeoffs in terms of computational complexity. Finally, the accuracy of the tomographic inversion technique in stellarator geometry is investigated, providing for the first time a verification exercise for inversion accuracy in with stellarator geometry and a complete XICS analysis tool-chain.

The X-Ray Imaging Crystal Spectrometer (XICS) is a primary diagnostic for time resolved temperature (T_i) and radial electric field (E_r) profiles on Wendelstein 7-X (W7-X)[1,2], and the only diagostic that can provide these core measurements during long pulse operation[3]. The analysis of the XICS data requires both spectral fitting and tomographic inversion, the latter of which is complicated by the 3D geometry of the W7-X stellarator. Due to the complexity of this analysis, a thorough verification of the procedure is needed to both ensure correct implementation and to understand the effect of approximations and assumptions in the analysis model. This type of verification study has recently become possible due to the development of a new advanced x-ray raytracing code, xicsrt, which allows simulation of the full plasma and diagnostic geometry while preserving accurate photon statistics[4]. This analysis allows the entire analysis tool-chain to be validated including all of the various built-in approximations.

The raytracing verification exercise presented here has led to the development of a number of important corrections that need to be applied to the standard analysis procedure. In particular, a correction to the T_i profile that reduces the temperature values by about $200\,\text{eV}$. These corrections were developed in June, 2019 and have been included in all T_i profile measurements presented in W7-X publications since that time. This is the first time that the full details of the correction

procedure have been published. The analysis presented here is specific to the system installed at W7-X, though many of the results are likely applicable to systems installed on other fusion experiments.

The verification study presented here is not a validation, and should not be interpreted as such. In particular the analysis in this paper does not validate any of the plasma physics, atomic physics models, or the system calibration. Instead, this verification is expected to serve as a starting point for a future validation and diagnostic cross-comparison exercise.

I. Diagnostic Description

The XICS diagnostic measures a one dimensional (1D) spatial profile of line-integrated emission spectra from highly charged argon impurities that are seeded into the plasma for diagnostic purposes[5,6]. The raw diagnostic output is a 2D image with energy dispersion in one direction and 1D imaging of the plasma in the other. Several plasma parameters can be measured from these spectra using standard Doppler spectroscopy techniques: ion-temperature (T_i) from the line widths, electron-temperature (T_e) from the line intensity ratios, perpendicular plasma flow velocity ($u_\perp$) from the line shifts, and impurity charge state densities (n_+) from the line intensities[7,5]. These measurements can be further used to infer the radial electric field profile (E_r) through radial force balance[8] and study impurity transport characteristics[9]. Tomographic inversion is used to find the local flux-surface plasma parameters from the line-integrated measurements[10].

There are three XICS systems installed on W7-X that allow simultaneous measurement of several impurity species

and charge states. The first system looks at the emission from Ar^{16+}, the second system looks at Ar^{17+}, Fe^{24+} and Mo^{32+}, and the third system (called the High Resolution X-Ray Imaging Spectrometer, HR-XIS) has a number of selectable crystals that can view different impurity species. A thorough description of the diagnostic hardware and capabilities can be found in Ref. 5, a description of the XICS analysis techniques can be found in Ref. 11.

A. Analysis Methods

There are two analysis methods that are currently used to interpret the raw XICS data at W7-X; for this paper we will call these the *multi-step* and *minerva* method[12]. The *multi-step* method performs the analysis in two steps: First the line-integrated data are fit using a physics based spectral model resulting in line-integrated values of line intensities , line widths and line shifts . Secondly the line-integrated parameters are tomographically inverted to find the local parameters on each flux surface[10]. The *minerva* method utilizes the MINERVA Bayesian analysis framework[13] to determine the local plasma profiles directly from the raw images through the use of a complete diagnostic forward model[12].

The *multi-step* analysis is computationally fast to perform, and is therefore well suited for routine analysis. However, this method requires a number of approximations; in particular the *multi-step* method makes the approximation that the sum of Voigt profiles that make up a line-integrated spectral line can be fit with a single Voigt profile and produce accurate values for the line moments. The *minerva* method avoids these approximations entirely and, in principle, can implement a model of arbitrary complexity and accuracy. The disadvantage is that the *minerva* analysis is computationally expensive, and currently infeasible for routine analysis. These two analysis methods agree very well in all cases that have been examined so far. The remainder of this paper will focus exclusively on the *multi-step* method.

II. X-Ray Ray Tracing using XICSRT

The raytracing for the current work has been enabled by the development of a new x-ray raytracing code. This code, named XICSRT, is a general purpose photon-based raytracing code capable of both optical and x-ray raytracing with an emphasis on plasma modeling and the preservation of photon statistics[14,15].

Of particular interest for the current work, XICSRT is capabile of modeling abitrarily complex 3D source geometries. In particular a module has been developed that allows the geometry from a stellarator VMEC equilibrium[16] to be used as x-ray source for raytracing. This source module allows the specification of plasma profiles for emissivity, ion-temperature and directional plasma flow. These parameters define a local non-isotropic wavelength distribution based on the Doppler broadening, Doppler shifts, and the natural line width.

To accurately model the emissivity, and to improve computational performance, the XICSRT source uses the concept of ray-bundles. Ray-bundles represent a small volume in the plasma with an emissivity and wavelelength distribution. To
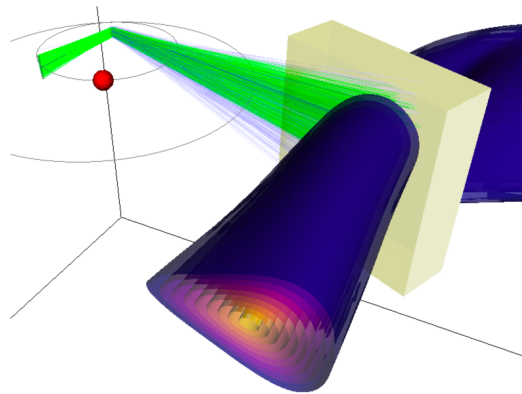

FIG. 1. *Visualization of raytracing in* XICSRT. *Green rays reach the detector, blue rays are launched but are not reflected by the crystal (A series of flux surfaces from a W7-X plasma equilibrium are plotted with the color scale from yellow to blue representing the normalized minor radius, ρ. The yellow box shows the volume from which rays are launched.*

launch rays from the source a large number of locations within the plasma volume are randomly sampled, and a ray-bundle is emmitted from each location. The number of rays launched from the bundle is randomly drawn from a continuous Poisson distribution based on the plasma emissivity, ray-bundle volume and a time-integration value. The wavelength of each ray within the volume is randomly selected from the local wavelength distribution. The individual rays within the bundle can be launched either from a point at the bundle location, or uniformly distributed inside a cube with the bundle volume (a voxel). The spatial accuracy of this source can be improved by increasing the number of ray-bundles. (The number of bundles and the bundle volume can be chosen independently; if so, a normalization of the emissivities is performed based on the total plasma volume to ensure the appropriate number of rays is launched that preserves overall photon emissivity.)

III. Line-integrated Analysis

The first step of this verification study is to look at the accuracy of the spectral fitting. Here only a simple ray source is needed: a slab plasma (or equivalently a sheet plasma) with constant emissivity, temperature and plasma flow. To verify the spectral fitting procedure only a single emission line, the w-line at 3.9492 Å, needs to be modeled. Raytracing is done using the best known calibrated geometry for the spectrometer including the finite crystal size of 40×100mm, and a detector with a pixel size of $172\,\mu m^2$ that matches the Pilatus 2 detector used in the experiment. A small number of background counts, randomly distributed according to a Poisson distribution, are added to the final images to simulate continuum emission (this also improves the assumption of normally distributed data inherent in the least-squares minimization). The images generated by XICSRT are formatted to exactly match the output from the physical detector and are saved in a virtual 'plasma shot'. This allows the output images to be analyzed identically to real W7-X data using the standard XICS *multi-step* automatic analysis tools. The difference between the input T_i and $u_\perp$ values in the simulation, and the subsequent fitted values can be seen in Fig.2. The ion-temperature shows

a clear overestimation of approximately 200 eV. This error in the fit of the spectral line width can be explained through three effects:

Decurving: The Ar16+ System at W7-X uses a detector with 195 pixels in the spectral direction and 1475 pixels in the spatial direction. The density of pixels in the spatial direction is much higher than needed given the native spatial resolution of the system as determined by the viewing volume in the plasma. For this reason it is useful to sum a number of rows on the detector before spectral fitting. This both improves signal to noise ratio during spectral fitting and greatly reduces computational time. Each of the spectral lines makes an ellipse on the detector and the dispersion of each row is slightly different. Before summation over a particular range of rows, each row be resampled onto a common wavelength grid (decurving). The algorithm used for this resampling makes an implicit approximation that the distribution of intensity within each pixel (in the spectral direction) is constant (first derivative is zero), and it is this assumption that leads an artificial broadening of the emission lines. This effect can be imagined as a kind of artificially introduced blurring of the spectral lines.

Fitting: Analysis of the spectra (for each spatial region after row summation) is carried out through the use of a atomic physics based forward model and fitting with a Levenberg-Marquardt least-squares optimization routine. The forward model is evaluated at a set of discrete wavelengths corresponding to the center of each (discrete) pixel. This means that the central intensity is assumed to be equal to the average intensity within the pixel and creates the implicit approximation that the intensity distribution within the pixel (in the spectral direction) is linear (second derivative is zero), leading to an overestimation of the line width, and therefore T_i.

Defocus & Aberrations: All XICS spectrometers are expected to have some line broadening from spherical aberrations and defocusing. With a planar detector it is not possible to achieve the best focus everywhere (the best focus lies on the surface of a sphere). In addition there will always be some instrumental broadening due to aberrations, dominated by the Johann error[17]. Both of these instrumental broadening effects increase with crystal size. The xicsrt raytracing is done using the calibrated spectrometer geometry and is expected to fully capture any defocus and aberration effects. In Fig.2(c) it can be seen that the error from *defocus & aberrations* is largest near the detector center, and decreases towards the edge. This is due to a particular alignment choice for the W7-X system in which the detector focus is calculated from the edge of the crystal (which is the center of the substrate) rather than the center of the crystal.

A small, but important, error in the fit of the line shifts (less than 0.1 mÅ) is also seen in Fig.2(b). This error is entirely due to abberations (Johann error) and is not affected by the sub-pixel intensity distribution.

A. Ion-Temperature Corrections

Raytracing of the system has been performed with a range of source temperatures ranging from 100 to 1500 eV to investigate the temperature dependence of the broading effects described above. As can be seen in Fig.2, no temperature dependence is seen over this range (this also holds for lower temperatures, however these data are not shown as the accuracy of spectral fitting is somewhat reduced as T_i approaches zero). This temperature independence enables a simple correction to be constructed from the raytracing results that can be applied after line-integrated spectral fitting. These corrected values can then be used in the tomographic inversion. Since the amount of broadening from the decurving effect depends on the number of rows being summed, a separate correction needs to be generated for each spatial binning scheme used. This same procedure is also used to correct the line-shifts, though this is a less important effect.

While it is possible to improve the forward model so as to remove the sub-pixel intensity distribution errors and include the instrumental response, doing so would require several orders of magnitude more computational time. For completeness, the required model improvements are nonetheless described here: The *fitting* errors can be addressed by evaluating the forward model at multiple points within each pixel and summing the results together (sub-pixel sampling); for the current system a sub-pixel sampling of 10 is sufficient. The *Decurving* error can be removed by either performing decurving as part of the model evaluation and taking into account the sub-pixel sampling evaluated above, or by avoiding summation of rows entirely by performing spectral/spatial fitting in two dimensions. Finally the instrumental response from *defocus & aberrations* can be incorporated into the forward model through convolution.

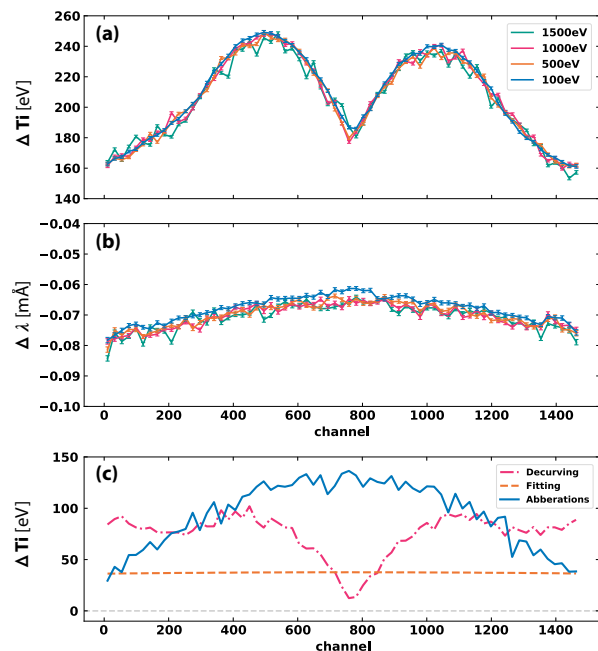Given the computational requirements for these model en-

FIG. 2. *a,b) Required corrections for ion-temperature and line-shift derived from raytracing and subsequent analysis. Raytracing was done using a simple slab plasma with several temperatures. Correction is derived by subtracting the input T_i and $V_\perp$ from the values derived through spectral fitting. Error-bars show the estimate of the 1-σ errors from the least-squares fitting procedure. c) Contributions of different broadening effects to the total T_i correction.*

hancements (which are multiplicative), utilization of the post-processing T_i correction is currently a better solution.

B. Experimental Application

To check that the ion-temperature corrections developed in Section III A are reasonable they are applied to experimental data from low temperature plasmas in W7-X. Normally low temperature plasmas (below $\approx$ 300-500 eV) are inaccessible to the XICS system because a minimum electron temperature is required to ionize argon to the Ar^{16+} charge state. However, in certain circumstances, such as with a small fully radiative plasma, charge exchange processes allow the Ar^{16+} state to exist at much lower plasma temperatures. The spectra obtained from these charge exchange spectra are unique in that they contain only the direct excitation lines w,x,y and z lines (no dielectronic recombination), and the line ratios of these lines are different what is seen from electron excitation (see Ref. 18).
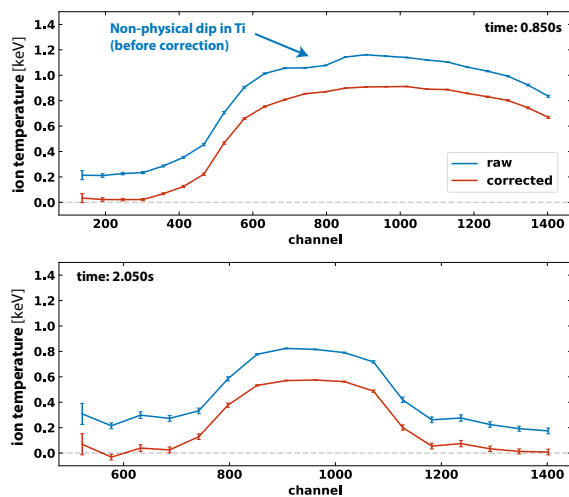

FIG. 3. *Line-integrated analysis of experimental Ar^{16+} XICS data from W7-X program 20171121.037. Blue curve is before application of the T_i correciton, red curve after application. Note that top and bottom plots have different x-axis (channel) scales.*

A search of all analyzed time slices from the first experimental physics campaign at W7-X (OP1.2) was performed to find a set of the lowest measured temperature profiles. The line-integrated T_i measurements from a low temperature W7-X plasma are shown in Fig.3 with and without the temperature correction applied. With the T_i correction enabled the lowest measured temperatures are reduced from 180 eV to 0 eV. Importantly the correction does not produce nonphysical negative T_i values anywhere (this is true for all W7-X profiles that have been measured to date). This means not only that these corrections are at least plausible, but also that they cannot be larger. Another important observation is that a nonphysical depression in the uncorrected T_i profile (seen around channel 750 in Fig.3) is completely removed in the corrected profile. Prior to the development of this correction, this T_i depression was seen in XICS measurement in all W7-X plasmas. That the T_i correction so effectively corrects the profile shape when applied to real data is a strong indication of its applicability.

IV. Tomographic Inversion

With the implementation of the T_i corrections described in Section III A the accuracy of tomographic inversion and the full *multi-step* analysis chain can be evaluated. To perform this study a more complicated raytracing geometry is needed that includes both the full 3D plasma shape and a set of plasma profiles. The W7-X plasma geometry is implemented in XICSRT using a VMEC equilibrium. For the results shown here a vacuum equilibrium for the *standard configuration* is used. Plasma profiles for Ar^{16+} emissivity and ion-temperature are modeled as flux surface functions. The model for the perpendicular flow velocity additionally includes a poloidal variation based on the theoretical expectation from flux-surface compression (see Ref. 6,19). The parallel plasma flow is set to zero for these simulations, to provide a better verification target. A set of profiles have been chosen that have a similar shape and magnitude to those found from experimental measurements.
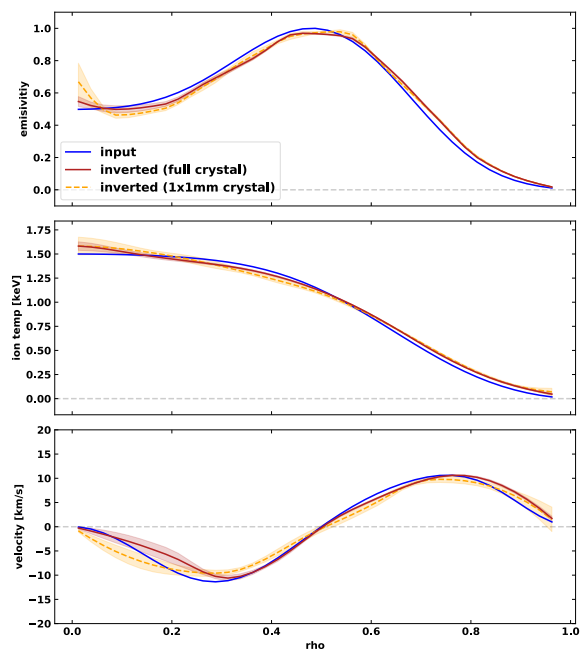

FIG. 4. *Results of the raytracing verification study including 3D stellarator geometry and realistic plasma profiles. Blue lines indicate the input profiles used for raytracing. Solid red curves show the results of XICS analysis of the raytracing output, including tomographic inversion. The shaded area represents one sigma errors in the analysis found using Monte-Carlo error determination. Dashed yellow curves show analysis of a raytracing run with a small (1×1mm) crystal size.*

The results from analysis of the raytracing output images, including Tomographic inversion are shown in Fig.4. Importantly these simulations capture any inaccuracies and approximations inherent in the *multi-step* analysis method. A second simulation and analysis performed with a small (1×1mm) crystal size shows identical results (within errorbars) and further highlights the the validity of the approximation of using line integrals for each binned 'sightline' rather than the true viewing volume. The ion-temperature and line-shift corrections described in Section III A have been applied in this analysis. The residuals from the analysis, in both the spectral

fitting and tomographic inversion steps, are within error-bars with reduced χ^2s around unity.

The emissivity profile is well reproduced, even in the hollow core; these profiles have been normalized to the integral curve, so while the shape can be compared absolute differences are not captured. The ion-temperature is also reasonably well reproduced within 50 eV of the original profile with the inverted temperature slightly over estimated in the edge and underestimated in the core. The perpendicular plasma flow is also well reproduced within error bars, including the radial location where the velocity profile transitions from positive to negative.

V. Conclusions

Advanced x-ray raytracing has been used to simulate XICS diagnostic signals on W7-X using realistic geometry for both the plasma and the diagnostic hardware. These simulated signals have then been analyzed using the same procedure as is used for experimental data, providing an end-to-end verification of the analysis procedure. In this processes, several corrections to the ion-temperature measurement were developed that arise from the subpixel-distribution of intensity within the pixels on the detector, which is not taken into account in the analysis model. These corrections are temperature independent, allowing them to be applied as part of the standard analysis procedure without loss of accuracy. With the correction applied the analysis of the simulated data reproduces the input ion-temperature and perpendicular plasma flow profiles closely. This analysis provides a measure of confidence in the *multi-step* method of analysis for the XICS system for typical W7-X plasmas.

While this verification exercise provides understanding about the accuracy of current analysis methods and their application to stellarator plasma geometries, it should not be mistaken for a diagnostic validation. In particular, the atomic physics model used in this analysis is not tested here, nor are other plasma physics assumptions that are built into the forward model. Indeed, even after implementation of the T_i correction described here, a discrepancy between the XICS measurements and those from other diagnostics on W7-X remains (with the XICS T_i value appearing to be too high by an additional ≈ 200 eV). Further validation and diagnostic cross-comparison will be the subject of a future paper.

Acknowledgments

Data Availability

The data that support the findings of this study are available from the corresponding author upon reasonable request.

References

[1] T. Klinger, T. Andreeva, S. A. Bozhenkov, C. Brandt, R. Burhenn, B. Buttenschön, G. Fuchert, B. Geiger, O. Grulke, H. P. Laqua, N. A. Pablant, K. Rahbarnia, T. Stange, A. von Stechow, N. Tamura, H. Thomsen, T. Wegner, and R. Bussiahn, Nuclear Fusion **59**, 112004 (2019), accepted for publication.

[2] R. C. Wolf, A. Alonso, S. Äkäslompolo, J. Baldzuhn, M. Beurskens, C. D. Beidler, C. Biedermann, H.-S. Bosch, S. Bozhenkov, R. Brakel, H. Braune, S. Brezinsek, K.-J. Brunner, H. Damm, A. Dinklage, P. Drewelow, F. Effenberg, Y. Feng, O. Ford, G. Fuchert, Y. Gao, J. Geiger, O. Grulke, N. Harder, D. Hartmann, P. Helander, B. Heinemann, M. Hirsch, U. Höfel, C. Hopf, K. Ida, M. Isobe, M. W. Jakubowski, Y. O. Kazakov, C. Killer, T. Klinger, J. Knauer, R. König, M. Krychowiak, A. Langenberg, H. P. Laqua, S. Lazerson, P. McNeely, S. Marsen, N. Marushchenko, R. Nocentini, K. Ogawa, G. Orozco, M. Osakabe, M. Otte, N. Pablant, E. Pasch, A. Pavone, M. Porkolab, A. Puig Sitjes, K. Rahbarnia, R. Riedl, N. Rust, E. Scott, J. Schilling, R. Schroeder, T. Stange, A. von Stechow, E. Strumberger, T. Sunn Pedersen, J. Svensson, H. Thomson, Y. Turkin, L. Vano, T. Wauters, G. Wurden, M. Yoshinuma, M. Zanini, and D. Zhang, Physics of Plasmas **26**, 082504 (2019), https://doi.org/10.1063/1.5098761.

[3] M. Krychowiak, A. Adnan, A. Alonso, T. Andreeva, J. Baldzuhn, T. Barbui, M. Beurskens, W. Biel, C. Biedermann, B. D. Blackwell, H. S. Bosch, S. Bozhenkov, R. Brakel, T. Bräuer, B. Brotas de Carvalho, R. Burhenn, B. Buttenschön, A. Cappa, G. Cseh, A. Czarnecka, A. Dinklage, P. Drews, A. Dzikowicka, F. Effenberg, M. Endler, V. Erckmann, T. Estrada, O. Ford, T. Fornal, H. Frerichs, G. Fuchert, J. Geiger, O. Grulke, J. H. Harris, H. J. Hartfuß, D. Hartmann, D. Hathiramani, M. Hirsch, U. Höfel, S. Jabłoński, M. W. Jakubowski, J. Kaczmarczyk, T. Klinger, S. Klose, J. Knauer, G. Kocsis, R. König, P. Kornejew, A. Krämer-Flecken, N. Krawczyk, T. Kremeyer, I. Ksiazek, M. Kubkowska, A. Langenberg, H. P. Laqua, M. Laux, S. Lazerson, Y. Liang, S. C. Liu, A. Lorenz, A. O. Marchuk, S. Marsen, V. Moncada, D. Naujoks, H. Neilson, O. Neubauer, U. Neuner, H. Niemann, J. W. Oosterbeek, M. Otte, N. Pablant, E. Pasch, T. Sunn Pedersen, F. Pisano, K. Rahbarnia, L. Ryć, O. Schmitz, S. Schmuck, W. Schneider, T. Schröder, H. Schuhmacher, B. Schweer, B. Standley, T. Stange, L. Stephey, J. Svensson, T. Szabolics, T. Szepesi, H. Thomsen, J.-M. Travere, H. Trimino Mora, H. Tsuchiya, G. M. Weir, U. Wenzel, A. Werner, B. Wiegel, T. Windisch, R. Wolf, G. A. Wurden, D. Zhang, A. Zimbal, and S. Zoletnik, Review of Scientific Instruments **87**, 11D304 (2016).

[4] J. Kring, N. Pablant, A. Langenberg, J. E. Rice, L. F. Delgado-Aparicio, D. Maurer, P. J. Traverso, M. Bitter, K. W. Hill, and M. Reinke, Review of Scientific Instruments **89**, 10F107 (2018).

[5] A. Langenberg, N. Pablant, T. Wegner, P. Traverso, O. Marchuk, T. Bräuer, B. Geiger, G. Fuchert, S. Bozhenkov, E. Pasch, O. Grulke, F. Kunkel, C. Killer, D. Nicolai, G. Satheeswaran, K. P. Hollfeld, B. Schweer, T. Krings, P. Drews, G. Offermanns, A. Pavone, J. Svensson, A. Alonso, R. Burhenn, R. Wolf, and The W7-X Team, Review of Scientific Instruments **89**, 10G101 (2018).

[6] N. A. Pablant, A. Langenberg, A. Alonso, C. D. Beidler, M. Bitter, S. Bozhenkov, R. Burhenn, M. Beurskens, L. Delgado-Aparicio, A. Dinklage, G. Fuchert, D. Gates, J. Geiger, K. W. Hill, U. Höfel, M. Hirsch, J. Knauer, A. Krämer-Flecken, M. Landreman, S. Lazerson, H. Maaßberg, O. Marchuk, S. Massidda, G. H. Neilson, E. Pasch, S. Satake, J. Svennson, P. Traverso, Y. Turkin, P. Valson, J. L. Velasco, G. Weir, T. Windisch, R. C. Wolf, M. Yokoyama, D. Zhang, and W.-X. Team, Physics of Plasmas **25**, 022508 (2018).

[7] M. Bitter, K. Hill, D. Gates, D. Monticello, H. Neilson, A. Reiman, A. L. Roquemore, S. Morita, M. Goto, H. Yamada, and J. E. Rice, Review of Scientific Instruments **81**, 10E328 (2010).

[8] N. Pablant, A. Langenberg, A. Alonso, J. Baldzuhn, C. Beidler, S. Bozhenkov, R. Burhenn, K. Brunner, A. Dinklage, G. Fuchert, O. Ford, D. Gates, J. Geiger, M. Hirsch, U. Höfel, Y. Kazakov, J. Knauer, M. Krychowiak, H. Laqua, M. Landreman, S. Lazerson, H. Maaßberg, O. Marchuck, A. Mollen, E. Pasch, A. Pavone, S. Satake, T. Schröder, H. Smith, J. Svensson, P. Traverso, Y. Turkin, J. Velasco, A. von Stechow, F. Warmer, G. Weir, R. Wolf, and D. Z. and, Nuclear Fusion **60**, 036021 (2020).

[9] A. Langenberg, T. Wegner, N. A. Pablant, O. Marchuk, B. Geiger, N. Tamura, R. Bussiahn, M. Kubkowska, A. Mollén, P. Traverso, H. M. Smith, G. Fuchert, S. Bozhenkov, H. Damm, E. Pasch, K.-J. Brunner, J. Knauer, M. Beurskens, R. Burhenn, and R. C. Wolf, Physics of Plasmas **27**, 052510 (2020), https://aip.scitation.org/doi/pdf/10.1063/5.0004462.

[10] N. A. Pablant, R. E. Bell, M. Bitter, L. Delgado-Aparicio, K. W. Hill, S. Lazerson, and S. Morita, Review of Scientific Instruments **85**, 11E424 (2014).

[11] N. A. Pablant, M. Bitter, L. Delgado-Aparicio, M. Goto, K. Hill, S. Lazerson, S. Morita, A. Roquemore, D. Gates, D. Monticello, G. H. Nielson, A. Reiman, M. Reinke, J. Rice, and H. Yamada, Review of Scientific Instruments **83**, 083506 (2012).

[12] A. Langenberg, J. Svensson, O. Marchuk, G. Fuchert, S. Bozhenkov, H. Damm, E. Pasch, A. Pavone, H. Thomsen, N. A. Pablant, R. Burhenn, and R. C. Wolf, Review of Scientific Instruments **90**, 063505 (2019), https://doi.org/10.1063/1.5086283.

[13] J. Svensson and A. Werner, IEEE International Symp. on Intelligent Signal Processing (2007).

[14] XICSRT sourcecode (2021), https://github.com/PrincetonUniversity/xicsrt.

[15] XICSRT package (2021), https://pypi.org/project/xicsrt.

[16] S. Hirshman and W. van Rig, Computer Physics Communications **43**, 143 (1986).

[17] H. H. Johann, Zeitschrift für Physik A Hadrons and Nuclei **69**, 185 (1931), 10.1007/BF01798121.

[18] P. Beiersdorfer, M. Bitter, M. Marion, and R. E. Olson, Phys. Rev. A **72**, 032725 (2005).

[19] J. Arévalo, J. Alonso, K. McCarthy, and J. Velasco, Nuclear Fusion **53**, 023003 (2013).